Probing the Structure-Performance Relationship of Lithium-Ion Battery Cathodes Using Pore-Networks Extracted from Three-Phase Tomograms

To cite this article: Zohaib Atiq Khan *et al* 2020 *J. Electrochem. Soc.* **167** 040528

View the article online for updates and enhancements.

Probing the Structure-Performance Relationship of Lithium-Ion Battery Cathodes Using Pore-Networks Extracted from Three-Phase Tomograms

Zohaib Atiq Khan,[1,2] Pablo Angel Garcia Salaberri,[3] Thomas M. M. Heenan,[4,5,*] Rhodri Jervis,[4,5] Paul R. Shearing,[4,5,*] Dan Brett,[4,5] Ali Elkamel,[1,6] and Jeff T. Gostick[1,*,z]

[1]Department of Chemical Engineering, University of Waterloo, Waterloo, ON, Canada
[2]Department of Chemical Engineering, University of Engineering and Technology Lahore, Pakistan
[3]Department of Thermal and Fluids Engineering University Carlos III of Madrid, Spain
[4]Electrochemical Innovation Lab, Department of Chemical Engineering, University College London, United Kingdom
[5]The Faraday Institution, Quad One, Becquerel Avenue, Harwell Campus, Didcot, OX11 0RA, United Kingdom
[6]Department of Chemical Engineering and Gas Research Center, Khalifa University, Abu Dhabi, United Arab Emirates

Pore-scale simulations of Li-ion battery electrodes were conducted using both pore-network modeling and direct numerical simulation. Ternary tomographic images of NMC811 cathodes were obtained and used to create the pore-scale computational domains. A novel network extraction method was developed to manage the extraction of N-phase networks which was used to extract all three phases of NMC-811 electrode along with their interconnections Pore network results compared favorably with direct numerical simulations (DNS) in terms of effective transport properties of each phase but were obtained in significantly less time. Simulations were then conducted with combined diffusion-reaction to simulate the limiting current behavior. It was found that when considering only ion and electron transport, the electrode structure could support current densities about 300 times higher than experimentally observed values. Additional case studies were conducted to illustrate the necessity of ternary images which allow separate consideration of carbon binder domain and active material. The results showed a 24.4% decrease in current density when the carbon binder was treated as a separate phase compared to lumping the CBD and active material into a single phase. The impact of nanoporosity in the carbon binder phase was also explored and found to enhance the reaction rate by 16.8% compared to solid binder. In addition, the developed technique used 58 times larger domain volume than DNS which opens up the possibility of modelling much larger tomographic data sets, enabling representative areas of typically inhomogeneous battery electrodes to be modelled accurately, and proposes a solution to the conflicting needs of high-resolution imaging and large volumes for image-based modelling. For the first time, three-phase pore network modelling of battery electrodes has been demonstrated and evaluated, opening the path towards a new modelling framework for lithium ion batteries.

Lithium-Ion batteries (LIBs) are the most widely used electrochemical energy storage devices for portable electronics and electric vehicles (EVs). They offer a good trade-off in terms of energy density, cycle life, low weight, low self-discharge, and high power-density and these advantageous properties have driven the revolution in portable electronics and, more recently, EVs. However, there is a continual need to improve their realizable energy density, enhance their safety, and extend their lifetime[1] as well as to reduce their cost. The positive electrodes in LIBs are composed of active material (typically a layered metal oxide material) into which Li-ion intercalation/deintercalation occurs, and a conductive additive (usually carbon black) that improves electrical conductivity throughout the electrode. These two components are combined with a binder into a porous structure and the remaining void space is filled with Li^+ containing electrolyte, creating a 3-phase porous electrode. Understanding the multiple, coupled transport processes within this porous electrode is key to enhancing the transport of Li ions and electrons, and hence to optimise design of LIBs.

To this end, mathematical modelling techniques are an essential tool to guide the experimental development of novel electrode structures. On one end of the spectrum lie the volume-averaged models originally developed by Newman et al.[2] The majority of these efforts focus on developing more accurate and/or complete continuum scale models that require less computational cost.[3,4] The drawback of continuum models is that they only include the microstructural properties of porous electrodes through volume-averaged correlations, but it is well known

that structure plays a key role in the species transport and ultimately device performance. At the other end of the spectrum, models based on direct numerical simulation (DNS) techniques using 3D images of the electrode microstructure as the computational mesh have been developed.[5–7] The relatively recent growth in application of 3D X-ray tomographic imaging to electrochemical devices and DNS models[8,9] have greatly enhanced the understanding of transport processes occurring inside the electrode by capturing details of the geometrical structure; however, DNS is computationally expensive. To incorporate all the necessary multiphysics, as well as transient behavior, is prohibitively demanding, such that even simulating the entire thickness of the cathode (on the order of 30–75 μm) is an unreasonable task. Thus only DNS of small sections of electrode can be undertaken, and these are not large enough to be representative of a real LIB. There is thus a strong need to develop a modeling framework that can bridge the gap between the continuum models of entire devices and DNS on subsections of microstructure, but at low computational expense while maintaining the crucial microstructural details. To meet this objective, pore network models are a promising option.

Briefly, pore network modelling is a method whereby a porous material is abstracted as a network of nodes and interconnections that represent pores and throats. It is possible using image processing to extract geometrical and topological details of porous media from a tomography image, then map this onto a network of interconnected nodes. Each node is a single unknown to be solved for, which approximates some of the pore-scale details of electrodes but allows simulation of large porous domains with very low computational cost as compared to DNS, with minimal difference in output (if the network extraction is performed correctly). Recently, pore network modelling has been used to model various electrochemical energy

conversion and storage devices. For example, Aghighi et al.[10] developed a pore network model to simulate a polymer electrolyte fuel cell (PEMFC) membrane electrode assembly. Aghighi et al.[11] later extended this model to measure the effect of phase change in a PEMFC cathode. El Hannach et al.[12] developed a pore network model to analyze water management and electrical performance of a PEMFC cathode catalyst layer. Their model discussed both pore and solid-phase networks and integrated different transport phenomena as well as electrochemical reactions in the catalyst layer. Similarly, pore network models have been utilized to study multiphysics transport processes in redox flow batteries (RFB)with the recent work of Sadeghi et al.[13] that developed a multiphysics pore network model to study the impact of electrode microstructure in redox flow batteries (RFBs). Gayon Lombardo et al.[14] used an X-ray CT image of a RFB electrode to extract a topological equivalent pore network and studied transient convective and diffusive transport processes. The results showed that concentration and pressure distribution inside electrodes greatly depends on microstructural properties. Some volume averaged approaches has also been adopted for fuel cell recently.[15,16] Together these recent works illustrate a new trend toward more complex multiphysics modeling using PNMs.

To date no PNMs have been applied to Li-ion battery electrodes. Lagadec et al.[17] have simulated the diffusion of Li-ions through a porous membrane separator, but they did not investigate the electrode structure or electrochemical reactions. Torayev et al.[18] used a pore network model of Li-O_2 batteries. They applied their model to four different regions of the electrode and found that galvanostatic discharge curves in each region varied significantly in terms of capacity and overpotential, supporting the notion that pore interconnectivity and macroscopic arrangement play a crucial role in performance. In another article, Torayev et al.[19] compared the ability of continuum and pore network modelling techniques to measure the impact of discharge performance and electrode pore size in Li-O_2 batteries. They concluded that continuum models should be used with caution as they are unable to capture important microstructural effects. It was also noteworthy that the pore network model, which explicitly captured pore interconnectivity, matched more closely with experimental data. These two studies were performed on the 3D reconstruction of super-P carbon electrodes with only pore and solid phase under consideration. Commercial lithium-ion battery cathode electrodes consist of three phases; electrolyte, carbon binder domain (CBD) and active material such as lithium iron phosphate (LiFePO$_4$, or LFP), lithium nickel manganese cobalt oxide (LiNiMnCoO$_2$, or NMC) and lithium cobalt oxide (LiCoO$_2$, or LCO). Treating the solid carbon binder and active material phases separately cannot only change the measured active surface area available, but also the transport mechanism of electrons in the solid phase because of significantly higher conductivity of the carbon binder domain (CBD) compared to active material.[20] Assuming carbon binder and active material as a single solid phase can significantly alter the electrochemical performance of the model. Hence, a computationally efficient pore network model is required that includes all the three phases with interphase and intraphase connectivity taken into consideration. As such, tomographic images containing all three phases are also essential.

The main objective of the present work is to apply and validate pore network modelling for studying the multiphysics involved in three-phase porous lithium-ion electrodes. A network extraction algorithm was developed to extract an arbitrary number of phases from X-ray CT images. The developed extraction algorithm is a continuation of previous work[21] and is used here to extract a topologically mapped network from a ternary tomogram of a LiNi$_{0.8}$Mn$_{0.1}$Co$_{0.1}$O$_2$ (NMC-811) electrode. The pore network was then used to simulate diffusion of lithium-ions in the electrolyte phase, conduction of electrons in active material and carbon binder phase and the reaction of lithium and electrons at the interface of active material and electrolyte phases of the porous cathode. Finally, two case studies are performed to highlight the importance of simulating three-phase lithium-ion cathodes and the influence of the

CBD nanopores on maximum attainable current density and voltage distribution. The presented pore network model provides a new avenue to study critical transport and reaction process in lithium-ion battery porous electrodes. To the best of our knowledge, this is the first network extraction of a lithium-ion battery cathode. The algorithm is written in python and is shared in the open-source project PoreSpy[22] available at https://github.com/PMEAL/porespy.

Methodology

Electrode material.—The material explored in this work is a nickel-rich lithium-ion cathode: Li(Ni$_{0.8}$Mn$_{0.1}$Co$_{0.1}$)O$_2$ or NMC-811, and was fabricated by Targray (18105 Transcanadienne, Kirkland QC, H9J 3Z4, Canada) via printing from a slurry onto an aluminum current collector and subsequently calendared to reduce electrode porosity. Additional information provided by the supplier can be found within the supplementary material (available online at stacks.iop.org/JES/167/040528/mmedia).

X-ray computed tomography.—To prepare the sample for imaging, a disk ca. 1.0 mm in diameter was punched from the electrode sheet and fixed atop of a 1.0 mm diameter, 10.0 mm tall steel dowel using quick-set epoxy. A single X-ray tomogram was collected using a Versa micro-CT instrument (Zeiss Xradia 520 Versa, Carl Zeiss., CA, U.S.A.). Imaging was conducted with a source accelerating voltage of 80 kV at a power of 7 W using a tungsten target for an un-filtered, polychromatic emission with a characteristic peak at 58 keV. The tomogram was collected using 3201 radiograph projections, each with an exposure of 16 s. Geometric magnification coupled with a scintillator and 20× optical magnification resulted in an image with a pixel size of 400 nm. These radiographs were then reconstructed using standard cone-beam, filtered-back-projection (FBP) algorithms using commercial software ("Reconstructor Scout-and-Scan," Carl Zeiss., CA, U.S. A.). After reconstruction, the tomogram data was processed using a non-local means filter to improve the image quality for segmentation. The data was then cropped, the greyscale values were segmented according to cathode particles (NMC811), binder and void/pore space. Further information on the quality of the image contrast, filtering and segmentation can be found in the supplementary material. All filtering, cropping and segmentation was achieved using Avizo Fire software (Avizo, Thermo Fisher Scientific, Waltham, Massachusetts, U.S.).

Pore network extraction.— *N-phase extraction algorithm.*—The developed network extraction algorithm is based on the watershed segmentation technique which defines the porous regions and throat connectivity in a visually intuitive manner.[23,24] The current algorithm is based on our previously published SNOW algorithm (Sub-Network of an Over-segmented Watershed)[25] and its extension SNOW_DUAL algorithm.[21] The basic SNOW algorithm consists of two steps. Firstly, marker-based watershed segmentation is performed to partition the image into pore regions. Before applying this step, however, spurious markers are trimmed by applying several filters (Fig. 1a) to avoid over-segmentation by the watershed filter. Secondly, the discretized regions are further analyzed one at a time to extract geometrical and topological properties of the pore regions. The basic steps involved in the network extraction process are shown in Fig. 1a. The SNOW algorithm was later extended to the SNOW_DUAL algorithm to extract both solid and void phases and, crucially, the interlinking of these phases with each other to study transport and reaction mechanisms in catalyst packings. However, lithium-ion cathode material consists of three phases, namely active material, CBD and electrolyte phase. Therefore, the dual approach was generalized to an N-phase extraction algorithm which can be applied to any material with an arbitrary number of phases. The developed model can be used for any kind of commercial cathode material such as lithium iron phosphate (LiFePO$_4$) and lithium
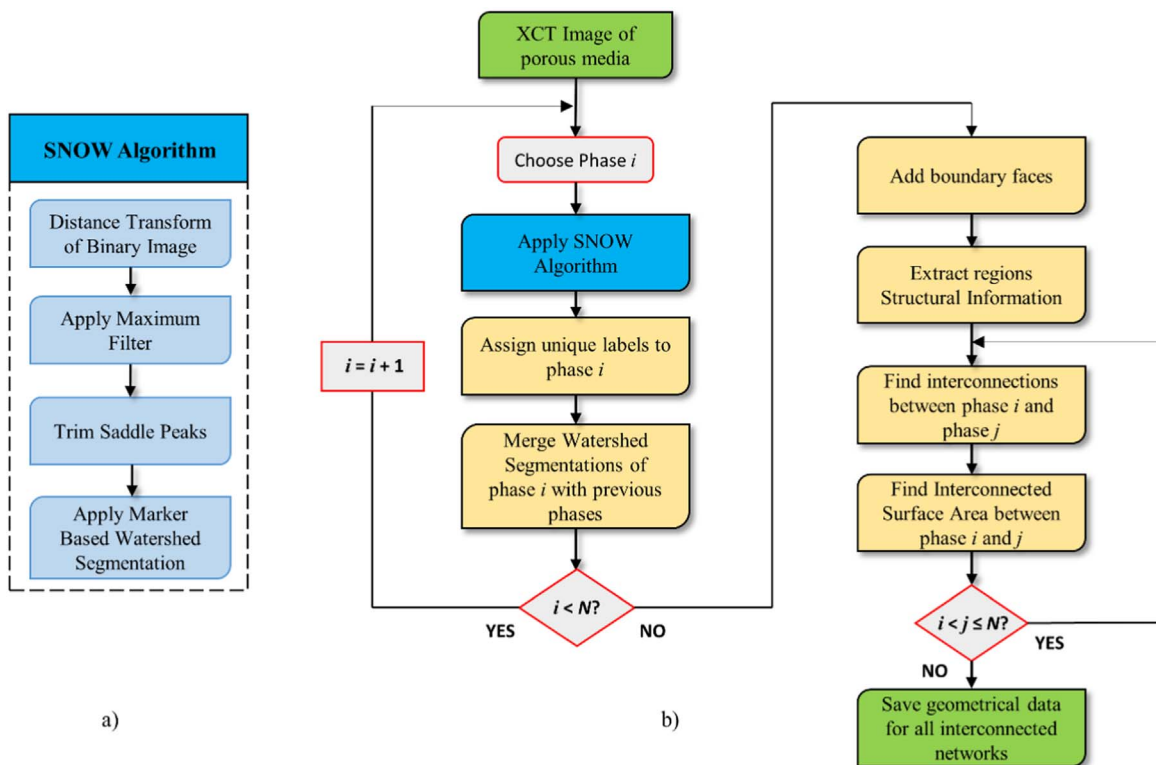
Figure 1. (a) SNOW algorithm basic steps (b) SNOW_N extraction algorithm flow chart.

cobalt oxide (LiCoO$_2$) if 3-phase tomograms were provided—or indeed for any tomographic data set of N-segmented phases.

The N-phase network extraction algorithm (SNOW_N) was developed on the premise that the watershed segmentation can be applied on each phase in an image individually, and then these individual segmentations can be combined to form a composite image. The overall algorithm implementation is shown in Fig. 1b.

Firstly, each phase (1 to N) is partitioned into regions using the SNOW algorithm individually. Before recombining the segmentations, the partitioned regions of the *jth* phase are relabeled in order to differentiate it from other phases. For this, if Np$_i$ is the maximum label of *ith* phase region then *jth* phase first label will begin from Np$_i$ + 1. After the relabeling process, all partitioned regions are merged together to form a composite watershed segmentation image. In the
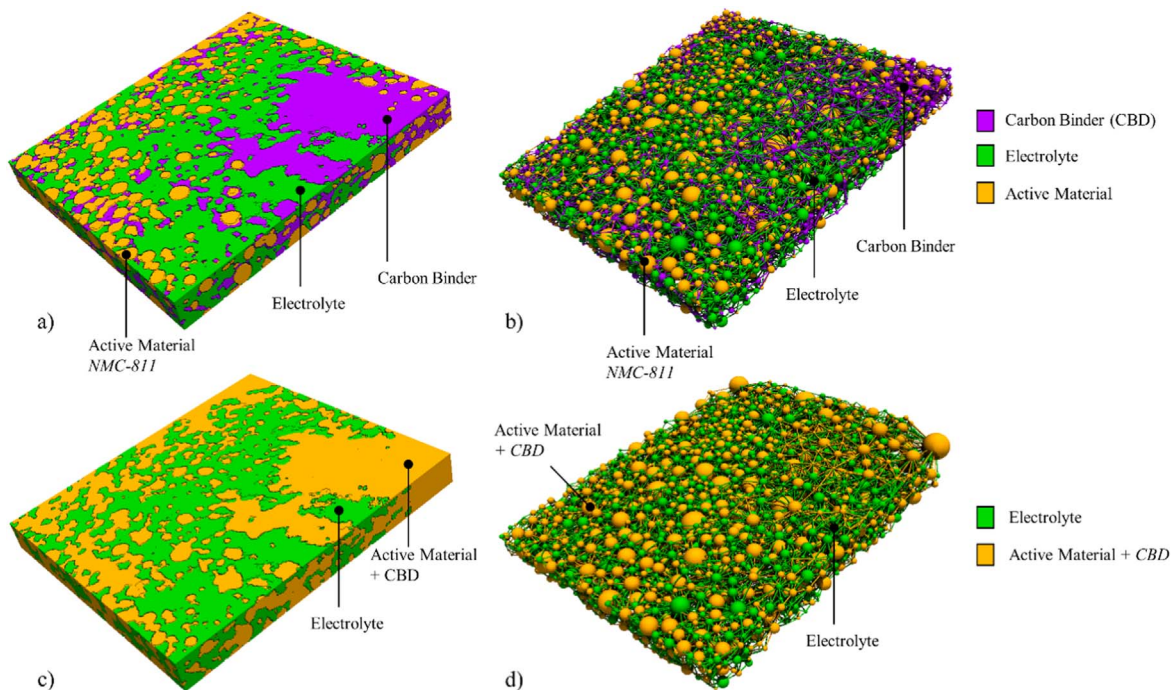
Figure 2. (a) X-μCT image of lithium nickel manganese cobalt oxide (LiNi$_{0.8}$Mn$_{0.1}$Co$_{0.1}$O$_2$) cathode, (b) Extracted three phase network of (a), (c) Two phase image of porous cathode where active material and CBD correspond to one solid phase, (d) Extracted two phase network of (c).

next step, boundary nodes are added to specify boundary conditions during the simulation process.[21] After assigning boundary nodes, the geometrical and structural features of each region are extracted one at a time without considering its phase association. The connectivity of the region under consideration is determined by scanning its neighbouring regions. This allows extracting throat properties of connected regions, including pore-to-pore, pore-to-CBD, binder-to-NMC, and so forth. Once all the geometrical and connectivity information is determined, the next step is to label the interconnections between each phase with other phases. This step finds throats that interlink any two phases with each other and stores it in the form of separate arrays. For N phases there will be NC_2 interconnection arrays. Next, the interfacial area between any two phases is determined using the marching cube algorithm which has been demonstrated to produce much more accurate values for interfacial area between regions.[21] Lastly, the extracted information is stored in the form of a Python dictionary which can be opened directly in the open-source modelling package OpenPNM.[26] The code is implemented in Python and is included in the open-source package PoreSpy.[22]

To illustrate the impact of treating the binder and active material as a single phase, the developed SNOW_N algorithm was used to extract both two-phase and three-phase networks of the Li-ion NMC-811 cathode. The two-phase network was extracted by assuming the carbon binder domain (CBD) and active material phase as one solid phase. The extracted networks are shown in Fig. 2. The green, purple and orange colour shows electrolyte, carbon binder and active material phase, respectively. The pore and particle size distribution for all phases is shown in Fig. 3 and properties of both networks and original image are presented in Table I.

Network validation by direct numerical simulation.—The SNOW network extraction algorithm has been previously validated for sandstone, fibrous media, and artificial foams (Voronoi tessellations),[25] and the SNOW-dual was validated for sphere packs,[21] but it is still necessary to validate 3-phase extraction on the present Li-ion battery material image. The triple phase nature of the material (and its requirement for a triple phase boundary to exist) leads to specific sensitivities of the modelling.

The most direct validation is obtained by performing direct numerical simulation (DNS) on the image using a finite volume approach. This provides reference values for effective diffusivity of the pore space (i.e. tortuosity) and effective conductivity of the solid phase (including both NMC and CBD particles). These values can then be compared to those predicted by the extracted network to ensure that it accurately represents the porous structure. The following sections detail the procedure used to obtain the DNS results.

DNS model formulation.—The predictive capabilities of the pore-network model were validated against the results computed by a DNS model, implemented in the FVM-based code ANSYS Fluent. The numerical domain was created using a direct mapping between the voxel image of the electrode and a hexahedral mesh generated with the same resolution (23,591,880 cells). Species and charge conservation equations (i.e., Laplace equation) were solved via user-defined scalars to determine the lithium-ion concentration and electronic potential, respectively. Therefore, the governing equation is given by

$$\nabla \cdot (\Gamma \nabla \phi) = 0 \qquad [1]$$

where Γ is either the mass diffusivity or electrical conductivity, and ϕ is the corresponding solution variable. In all cases, the Laplace equation was discretized in ANSYS Fluent using second-order central difference.

Several user-defined functions were used to customize the model, including boundary conditions, transport properties and output results. The material properties and boundary conditions were similar to those prescribed in the pore-network model. The only difference is that boundary conditions were also set at internal interfaces. Consequently, in the reaction-diffusion simulation, zero concentration was imposed at the electrolyte/active material interface to model limiting-current conditions, rather than prescribing a high reaction-rate constant at electrolyte/active material interface (as done in the pore-network model described below). Similarly, in the reaction-conduction simulation, current density at the electrolyte/active material interface was determined by direct application of Faraday's law on the interfacial diffusive flux determined previously. A no-flux boundary condition was set at the electrolyte/CBD interface, while a coupled (i.e., continuity) boundary condition was prescribed at the active material/binder interface.

Pore-network formulation.—The present study focuses on the cathode electrode of Li-ion battery that includes current collector and lithium nickel manganese cobalt oxide ($LiNi_{0.8}Mn_{0.1}Co_{0.1}O_2$) porous cathode operating under pseudo steady-state conditions. Figure 4 illustrates the schematic of a cell of lithium-ion battery domain. During discharge, lithium ions travel from the membrane side, through the electrolyte phase (pores) and intercalate into the active material (NMC-811) surface to form lithium nickel manganese cobalt oxide according to following electrochemical reaction:

$$x\text{Li}^+ + xe^- + Li_yNi_{0.8}Mn_{0.1}Co_{0.1}O_2 \rightarrow Li_{x+y}Ni_{0.8}Mn_{0.1}Co_{0.1}O_2 \qquad [2]$$
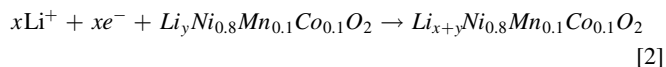
The physical processes occurring in the lithium-ion battery cathode during discharge are (a) diffusion and migration of lithium-ions in the electrolyte phase, (b) conduction of electrons in the active material and carbon binder domain and (c) reaction (i.e., intercalation) of lithium-ion at the interface of electrolyte and active
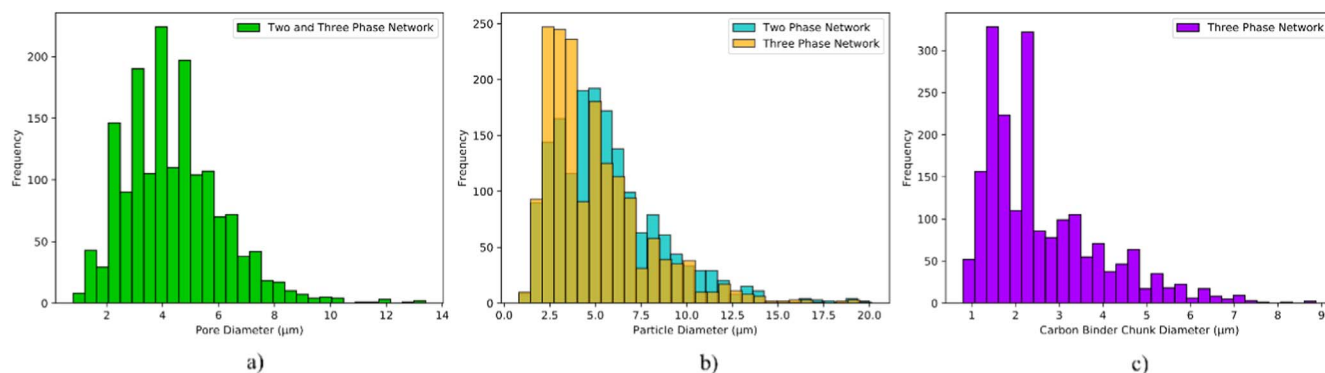
Figure 3. (a) Pore size distribution of electrolyte phase in both two and three phase network, (b) Active material particle size distribution in two and three phase network, (c) Carbon binder particle size diameter in three phase network.

Table I. Properties of image and extracted pore networks.

Value	X-μCT image	Three Phase Network	Two Phase Network
Dimension [voxels]	568 × 639 × 65	568 × 639 × 65	568 × 639 × 65
Voxel Size [nm]	400	400	400
Phase [vol %]			
1. Electrolyte	38.6	38.23	38.1
2. Active Material	39.6	39.53	61.9
3. Carbon Binder	21.9	22.23	—
Electrolyte Phase: N_p, N_T	—	1648, 3619	1648, 3619
Active Material Phase: N_p, N_T	—	1712, 2057	1726, 5316
CBD Phase: N_p, N_T	—	1976, 4227	—
Interconnections:			
1. Electrolyte-Active Material	—	6888	11419
2. Electrolyte-CBD	—	8878	—
3. Active Material-CBD	—	7435	—
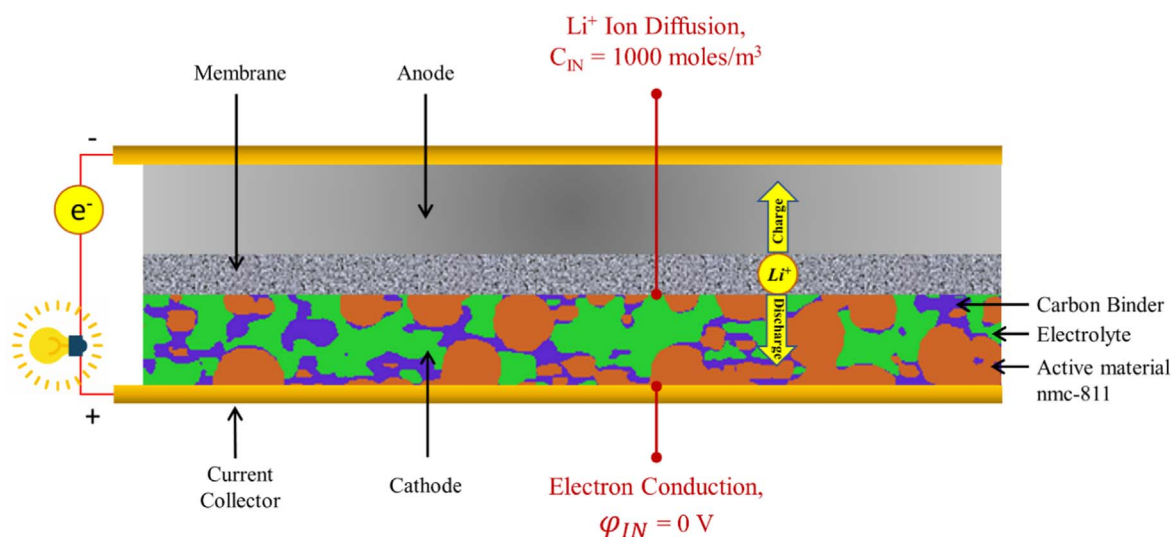
Figure 4. Schematic diagram of full cell lithium Ion battery. The applied boundary conditions are shown in red color.

material. Several simplifying assumptions were made in this work since the focus was on the pore-scale transport processes rather than complete battery operation. The generation and transport of heat were neglected, as were any side reactions such as SEI formation. Migration of ions due to electric fields were also neglected. Electrochemical kinetics were not included, but rather it was assumed that the kinetics of the lithium intercalation reaction were very fast on the surface of the active material. This assumption simplifies the problem by decoupling the electrolyte and solid phase potentials, reducing it to reaction-diffusion in the electrolyte phase and reaction-conduction in active material phase. It was also assumed that effective transport properties are not concentration dependent as recently suggested in.[27,28] We assume all transport properties to be constant with changing concentration. The extension of this model to transient conditions relevant to charging and discharging will also be left for future work. The transport and kinetic equations that were used in the developed pore network model are given in the following sections.

Lithium-ion transport.—The lithium ion transport in the electrolyte phase was considered to follow a reaction-diffusion process during the discharge cycle of the battery. The conservation of lithium-ions around a pore *i* in pore network under steady-state conditions can be represented by:

$$\sum_{j=1}^{N_i} q_{i,j} = R_i = kc_i \tag{3}$$

where *q* is the molar flow rate in mol/s. R_i is the net reaction rate of Li-ions in pore *i*. *k* refers to the reaction constant and c_i refers to the concentration of Li-Ion in pore *i*. N_i is the number of neighbour pores to pore *i*.

The molar flow rate q_{ij} between pore *i* and *j* can be defined using 1D Fickian diffusion:

$$q_{i,j} = \frac{D_{Li^+}A}{x_{i,j}}(c_i - c_j) = d_{i,j}(c_i - c_j) \tag{4}$$

where D_{Li^+} is the bulk diffusion coefficient of Li$^+$ ions in the electrolyte phase. *A* is the cross-sectional area of conduit from pore *i* to pore *j*, $x_{i,j}$ is the length of conduit from pore *i* to pore *j*, c_j is the concentration of Li ion in the neighbouring pore *j* and $d_{i,j}$ is the diffusive conductance between pore *i* and *j*.

Electron transport.—The charge conservation for an arbitrary solid particle *i* is represented by the following governing equation:

$$\sum_{j=1}^{N_i^{AM}} I_{i,j} = R_i^e = z \cdot F \cdot R_i \qquad [5]$$

where $I_{i,j}$ is the rate of charge transport from solid particle i to solid particle j in Coulombs s^{-1}. R_i^e is the net reaction rate of electrons at surface of particle i. F is Faraday's constant and z is the number of electrons.

The rate of charge transport is proportional to the potential difference between particle i and j as stated by Ohm's law:

$$I_{i,j} = \frac{\sigma_e A}{l_{i,j}}(\varphi_i - \varphi_j) = \sigma_{i,j}(\varphi_i - \varphi_j) \qquad [6]$$

where ϕ_i and ϕ_j are the electric potentials in active material at particle i and j respectively. σ_e is the bulk electronic conductivity of active material (NMC-811). $l_{i,j}$ is the conduit length from particle i and j. $A_{i,j}$ is the cross-sectional area of the conduit. $\sigma_{i,j}$ is the electrical conductance between active material particle i and j.

It is assumed that no reaction takes place in the carbon binder phase. Therefore, the governing equation for charge conversation in this phase is as follows

$$\sum_{j=1}^{N_i^{CB}} I_{i,j}^{CB} = 0 \qquad [7]$$

The rate of charge transport in carbon binder phase can be represented as 1D Ohm's law under steady-state conditions as

$$I_{i,j} = \frac{\sigma_{CB} A}{k_{i,j}}(\varphi_i^{CB} - \varphi_j^{CB}) = \sigma_{i,j}^{CB}(\varphi_i^{CB} - \varphi_j^{CB}) \qquad [8]$$

where σ_e^{CB} is the electronic conductivity of carbon binder domain. φ_i^{CB} and φ_j^{CB} are potential difference in carbon binder region i and j respectively. $k_{i,j}$ is the conduit length in carbon binder region i and j respectively. The overall summary of the parameters used in this study is shown in Table II.

Boundary conditions.—The boundary conditions implemented for mass and current transport for different cases were as follows:

1. In the electrolyte phase, a Dirichlet boundary condition of 1000 mol m^{-3} concentration of lithium ions was assigned in inlet pores at the separator surface. For the simulation in which only effective diffusivity is calculated, a Dirichlet boundary condition of 0 mol m^{-3} at outlet pores (near the current collector) and zero-diffusive flux at solid/electrolyte interface was applied, while for reaction-diffusion simulation Neumann boundary condition of zero diffusive flux was set in the outlet boundary pores.

2. In the active material and carbon binder phase, 0 volt Dirichlet boundary conditions were implemented at the current collector. For simulations which calculate effective conductivities of the active material and carbon binder phases, 1 volt Dirichlet boundary conditions at outlet particles and zero-conductive flux at solid/electrolyte interface was applied, while for reaction-conduction simulation, Neumann boundary condition of zero flux of charge was implemented at outlet particles.

Pore-scale conductance models.—To calculate the transport rate between two pores i and j it is necessary to determine the total conductance of the conduit between the two pores, which consists of half of pore i, the throat, and half of pore j. In the present work, a custom geometrical model for the conductance of each pore was applied, based on truncated pyramids as shown in Fig. 5. Due to the generally spherical nature of the grains in the electrode (both NMC and CBD phases), the contacts between two pores essentially have no throat of length greater than zero. This overlapping sphere-sphere contact was modeled as the intersection of pairs of 4-sided truncated pyramids. The base of the pyramids was found from the diameter of pore, and the truncated side was set to the throat diameter. In this model, the conductance of the throat was assumed negligible because of zero length and the effect of the constriction between pores was included in each pore's contribution. The total conductance, G, in a conduit made up of pores i and j and throat k can be calculated since the resistances act in series:

$$\frac{1}{G_{i,j}} = \frac{1}{g_{i-k}} + \frac{1}{g_{j-k}} \qquad [9]$$

where g_{i-k} and g_{j-k} are found for each individual pore-throat section as described below.

This results in the following expression for the electrical conductance of pore i connected to throat k:

$$g_{i-k}^e = \sigma \frac{d_i d_k}{L} \qquad [10]$$

where d_k is the diameter of throat, L is the distance from centroid of pore i to centroid of throat k and d_i is the diameter of pore i which is adjusted so that volume of truncated pyramid is equal to half of the volume of pore i.

The pore space is defined by the interstitial regions between grains of solid material. In this case, like the solid phase discussed above, the throats are essentially constrictions defined by the converging-diverging nature of the spheres. As such, the same truncated pyramid model was also applied:

$$g_{i-k}^d = \mathcal{D}_{Li^+} \frac{d_i d_k}{L} \qquad [11]$$

Table II. Summary of the parameters used in this study.

| Parameter	Value	Units	Description
$L_{cathode}$	2.6×10^{-5}	m	Cathode thickness
$A_{cross-section}$	5.807×10^{-8}	m^2	Cross-sectional area of cathode
$V_{cathode}$	1.51×10^{-12}	m^3	Volume of cathode
D_{Li^+}	1.81×10^{-10}	m^2.s^{-1}	Bulk diffusivity of Li ion in electrolyte phase[5]
σ_{CBD}	760	S.m^{-1}	Electronic conductivity of carbon binder phase[29]
σ_e	1.7×10^{-3}	S.m^{-1}	Electronic conductivity of NMC-811[30]
C_{IN}	1000	kg.m^{-3}	Concentration of lithium ion at membrane-cathode interface
φ_{IN}	0	Volt	Voltage at cathode current collector
F	96485	C.mol^{-1}	Faraday's constant
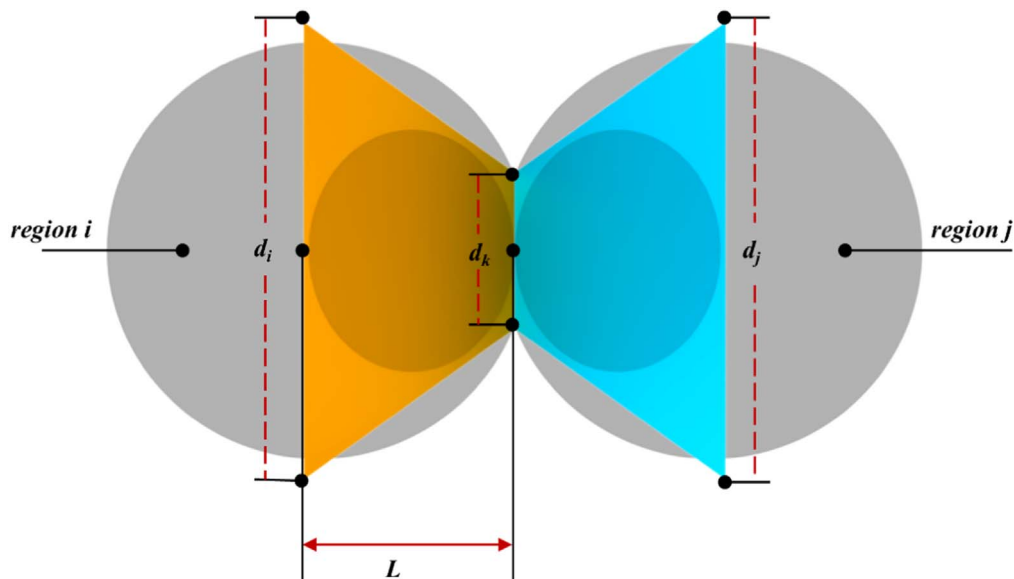
Figure 5. Schematic of geometric properties of pore scale conduit in network model.

where $\mathcal{D}_{Li^+}$ is the diffusion coefficient of the Li ion in the electrolyte and the geometrical properties are defined as above. All of the lengths and diameter values were determined during the network extraction stage described above.

Results and Discussion

PNM validation against DNS.—*Effective transport properties.*—The pore network model (PNM) results were compared with direct numerical simulations (DNS) for two different conditions. In the first case, effective transport properties were determined using both PNM and DNS in both the electrolyte and solid phase under steady state conditions. Dirichlet boundary conditions were used in both inlet and outlet pores as described in boundary conditions section. The comparison of results is shown in Table III. The combined effective conductivities in the active material and carbon binder phase were calculated using both approaches and the relative error was found to be approximately 3%. The normalized effective diffusivity of Li-ions in the electrolyte phase is 0.178 in PNM in comparison to 0.145 in DNS simulation, meaning that the PNM model overestimated diffusivity by 18.5% (taking the DNS result as correct), which is not as close as the solid phase, but still quite acceptable. These higher relative errors in this case of diffusion can be attributed to the simplification of irregular pore-scale conduit geometry to truncated pyramids, which evidently works better for the solid phase because it's generally spherical than the pore phase. Given that the pore network modelling approach takes significantly less computational time than DNS the relative errors reported in Table III are acceptable for performing engineering design and optimization calculations. The simulation results in terms of concentration and voltage profiles are compared for both cases in Fig 6.

*Comparison of computational costs.*—One of the benefits of pore network modelling over direct numerical method is low computational cost required for simulations. To study the computational cost of the simulations described above we have divided computational time in two parts. (1) Meshing or extraction time and (2) Problem solution time. In this study the approximate time taken to build 25.5 million mesh elements domain was 1 h. On the other hand, in pore network modelling the equivalent to meshing is extracting the network, which required approximately 5 min to extract 6460 nodes. However, when comparing the computational cost of running the simulations, the average solution time in DNS and PNM was 25 min and 1.21 s respectively. The computational time was calculated in Inter Xeon E5–2640, 2.40 GHz, 128 GB RAM and 20 Cores. For direct numerical simulation the solver was parallelized across 10 cores to achieve residual below 10^{-8} while PNM solution was calculated using only 1 core. This comparison highlights the major advantage of the PNM approach over DNS, especially while simulating large electrode domains. The comparative advantage of PNMs would become even more important when considering multiphysics such as migration of ions, and transient behavior.

Coupled electron conduction and diffusion-reaction.—With the pore-network extraction and geometrical representation validated by the comparison of overall effective transport properties above, the model was then used to predict the maximum achievable current density. For this study, reaction-diffusion of lithium-ions in the electrolyte phase and reaction-conduction of electrons in the active material and carbon binder domain phases were analyzed simultaneously in the presence of a fast reaction of Li-ions at the NMC phase surface, as discussed in pore network formulation section. This assumption forces Li-Ion reaction to follow first-order kinetics instead of Butler-Volmer kinetics as per Eq. 2. Although actual Butler-Volmer kinetics can be implemented in the PNM model,[13] the purpose of this work was to explore the impact of structure on the maximum performance of Li-ion cells, and to validate our PNM

Table III. Summary of results in this study.

Variable	Pore Network Model	Direct Numerical Model	Relative Error (%)
D_{eff}/D_{bulk}	0.178	0.145	18.5
σ_{eff}	31.9	30.92	3.07
Li$^+$ flux$_{void-NMC}$	1.481×10^{-2} mol m^{-2} s^{-1}	1.496×10^{-2} mol m^{-2} s^{-1}	0.67
$i_{void-NMC}$	1429.8 A m^{-2}	1411.7 A m^{-2}	1.26
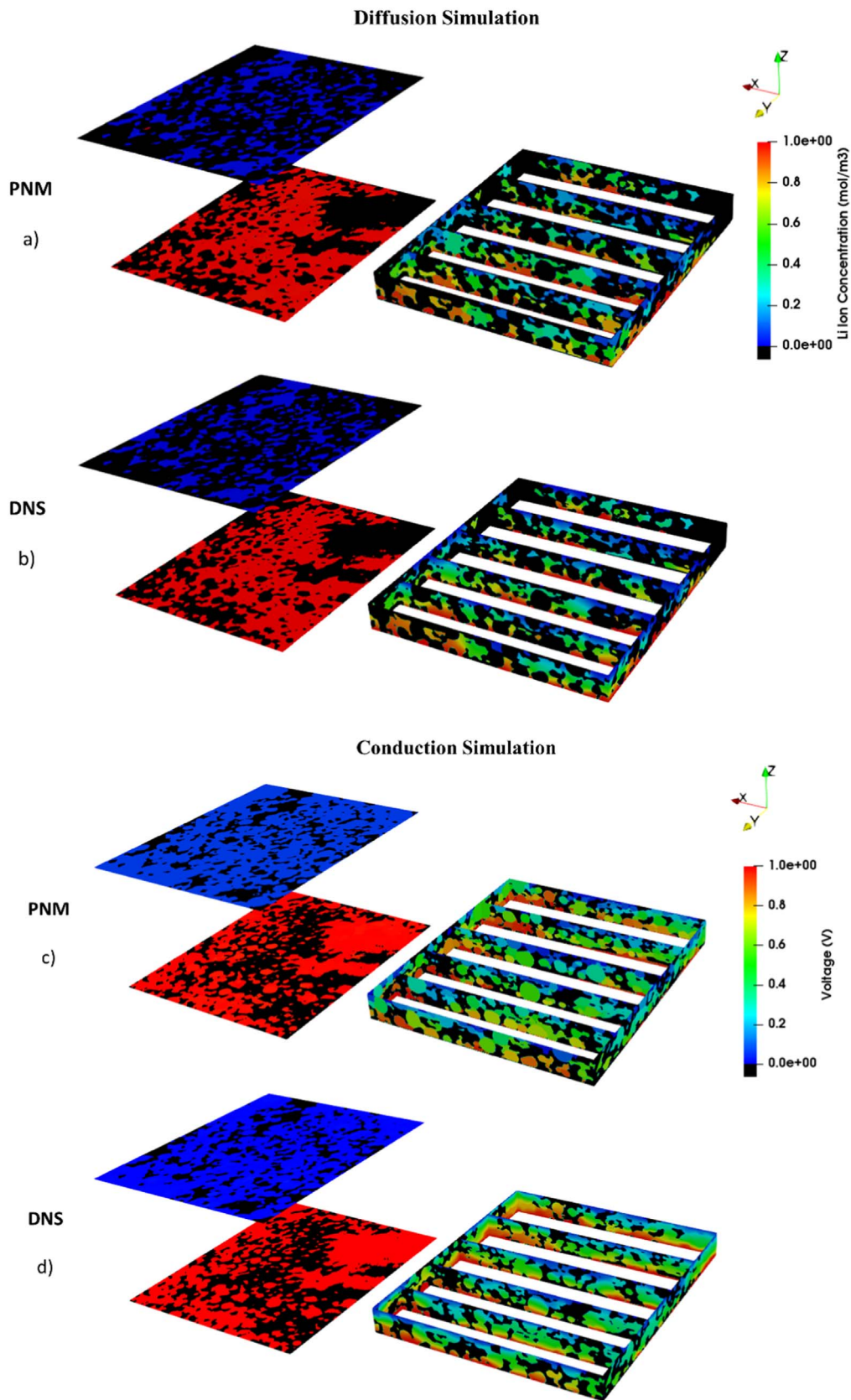
Figure 6. (a) and (b) Comparison of DNS and PNM model in pure diffusion simulation, (c) and (d) DNS and PNM model comparison in pure conduction simulation.

approach to solve lithium-ion battery problems as a foundation for future work. As can be seen in Table III, the PNM and DNS models

predict a maximum or limiting current density of 1.43 and 1.41 mA mm^{-2}, respectively. These values are substantially higher

than experimentally observed values, which are typically in the range of 1×10^{-3}–2×10^{-2} mA mm^{-2}.[5] It was expected that the present simulations would be higher than an operational battery since mass transfer limited conditions were forced by applying very high reaction rates at the electrolyte-active material boundary. Moreover, we did not consider that Li-ions must diffuse into the active material after intercalation occurs. It is actually quite instructive to note that the pore structure is capable of supporting such high current densities, and that the cumulative effect of the real phenomena not considered in this study hinder the reaction rate substantially. Adding more complexity to the pore network model in future work will be valuable for understanding the contribution of each process.

It is also observed that both the DNS and PNM simulations give very similar results for this case study. The average Li-Ion flux at electrolyte-active material interface differs by less than 1% between the PNM and DNS approaches. The results of the two approaches in terms of concentration and voltage distributions are shown in Fig. 7. From the results in Table III it can be visually confirmed that the PNM approach produces results well within acceptable error to be used as an alternative modelling method for simulating Li-Ion battery problems.

Impact of electrode structure.—Most pore-scale models of lithium-ion batteries in the literature treat the electrode as a two-phase system consisting of void and solid, meaning the active material and carbon binder domain are treated as a single phase. Given that carbon is specifically added to overcome the poor electrical conductivity of the active material, it is expected that such a simplification can produce erroneous results. This simplification was necessary since previously available tomography images only contained binary phase information. Attempts to work around this limitation have been made by algorithmically adding CBD to the solid phase.[31,32] The available of a true 3-phase image in the present work provides an opportunity to better understand the importance of treating CBD as a separate phase. he developed pore network was used to study two different cases described below.

Impact of treating carbon binder as a separate phase.—As described in N- phase network extraction section, the SNOW_N algorithm was used to extract both two and three-phase networks of lithium-ion cathode. The schematic diagram of both networks is shown in Fig. 2. These networks were used to perform comparisons of electrodes with and without carbon binder phase as shown in Fig. 3. Table IV shows the surface area, effective conductivities and current density calculated in both two-phase and three-phase network. As expected, the average particle size in the two-phase network is larger than the three-phase case due to the fact that carbon binder particles are lumped together with the active material.

As a limiting case, the maximum current density that can be supported by the structure was calculated by simultaneously modelling the diffusion of Li-ions with a rapid reaction in the active material. Limiting current may not be observed practice, but it is an interesting modeling target since it reveals that maximum current that can be supported by the electrode structure if electrolyte phase transport were the only source of mass transfer resistance. The current density was found by calculating the total rate in mol s^{-1} of Li-ions entering the domain from the membrane, converting to total current, I, using Faraday's law, then normalizing by the cross-sectional area of the current collector. As shown in Table IV the current density is 24.4% higher in the two-phase network compared to the three-phase case. This decrease when considering the CBD is due to the reduction in reactive surface area available when CBD is treated explicitly. It should be noted that the few studies which did treat the CBD as a separate phase used DNS. Due to high computational cost, these studies were limited to a domain volume of approximately 20.2 μm $\times$ 18.13 μm $\times$ 12.4 μm[5] compared to the electrode volume of 227.2 μm $\times$ 255.6 μm $\times$ 26 μm used in the current study; approximately 58 times larger when the voxel sizes

are considered. The volume limitation in the present work was not due to computational cost, but rather the field of view of the image. This has considerable implications for battery modelling—using a PNM approach it would be possible to model whole electrodes imaged via 3D stitching of several CT data sets without compromising on acquisition resolution.

The role of nanopores in the carbon binder phase.—It has been reported that nanoporosity of the carbon binder phase in the porous cathode affects overall ionic and electronic transport process.[20,31,33] This nanoporosity not only alters ionic diffusion pathways and access to the active material, but also affects the electron conducting network. To understand the importance of nanopores in the carbon binder phase, a parametric study was conducted where the porosity for the carbon binder was varied. These nanopores were not modelled explicitly as this would massively increase the computation demand of the model, negating the value of the PNM approach. Instead, the effect of nanoporosity was included by altering the effective conductivity and diffusivity of the CBD nodes in the network. To scale these transport parameters as a function of nanoporosity a Bruggeman-type relation was used,[34] given by Eqs. 12 and 13:

$$D_{CBD}^{Li^+} = \mathcal{D}_{Li^+}(\varepsilon_{CBD})^n \qquad [12]$$

$$\sigma_{eff} = \sigma_{CBD}(1 - \varepsilon_{CBD})^n \qquad [13]$$

where ε_{CBD} is the nanoporosity of the carbon binder phase, $\mathcal{D}_{Li^+}$ is the intrinsic diffusivity of Li-ion in electrolyte phase, σ_{CBD} is the intrinsic electronic conductivity of carbon binder phase. $\mathcal{D}_{Li^+,CBD}$ and σ_{eff} represent effective diffusivity and electronic conductivity after inclusion of nano pores in the carbon binder phase. n represents the Bruggeman constant which depends on how the nanopores are connected. Traditionally, $n = 1.5$ for a sphere pack, but is often higher for real random structures, so in this study n was varied between 1.5 and 3.

Figure 8 shows the impact of varying ε_{CBD} on various aspects of the electrode performance with n as a parameter. Figure 8a shows how the effective electrical conductivity of the entire network decreases as the nanopore fraction of the carbon binder increases. As $\varepsilon_{CBD} \rightarrow 1$ the electrical conductivity for the electrode nears 0 for all values of n, since the conducting carbon material is sacrificed. Figure 8b shows that the effective diffusivity of the network increases as ions are able flow through the nanoporosity. As $\varepsilon_{CBD} \rightarrow 0$ the effective diffusivity approaches the value obtained in 3.1.1 for the pore network. The electrolyte phase tortuosity $\tau_{Li^+} = \frac{\varepsilon D_{Li^+}}{D_{eff}}$ match well with recent study on LIB's transport "distortion".[35] It was observed that addition of high amounts of nanoporosity more than doubles the ability of Li ions to transport throughout the network. It is unlikely, however, that such high amounts of porosity could be achieved. Moreover, as already seen, high porosity drives the electrical conductivity of the network toward zero value so is not a practical target anyway. For both transport processes, the value n has only a small impact, except at low values of ε_{CBD}. For $\varepsilon_{CBD} < 0.2$, the effective diffusivity is almost unchanged while the electrical conductivity decreases noticeably. Note that Eqs. 12 and 13 do not include percolation effects, which would make this behavior at low ε_{CBD} even more pronounced.

More interesting is the interplay between increasing effective diffusivity and decreasing conductivity as the nanoporosity is increased. Simulations were performed with the ion diffusion-reaction coupled to the electron conduction, such that the voltage drop in each particle was determined that ensured a sufficient flow of electrons were delivered to each active site to match the consumption of ions there. Figure 8c shows the voltage of each NMC and CBD particle in the network as a function of position in the thickness direction of the electrode. These results were obtained for $\varepsilon_{CBD} = 0$ and $n = 3$. It can be seen that a small number of NMC particles
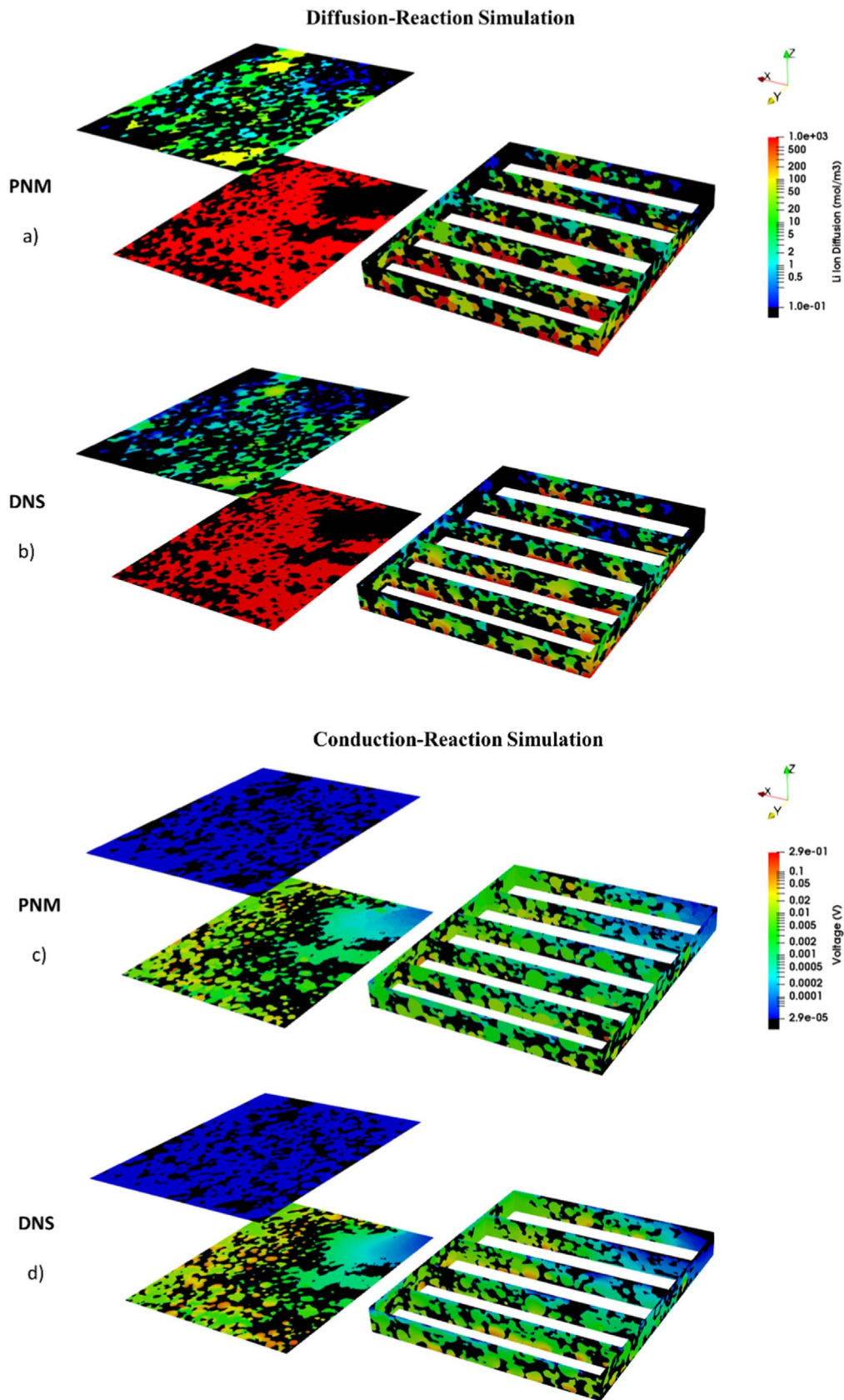
Figure 7. (a) Direct Numerical simulation of Li ion diffusion and reaction, (b) Pore network modelling simulation for same case as in (a), (c) Direct numerical simulation of conduction-reaction in active material and carbon binder phase, (d) Pore network modelling simulation of same case as (c).

display a high voltage. This may indicate that these particles suffer from artificially decreased connectivity with the current collector

due to edge effects from image cropping. None of these particles are fully disconnected (i.e. floating in space) as sometime occurs due to

Table IV. Summary of results in case study 1.

Variable	Units	Three Phase Network	Two Phase Network
$SA_{interface}$	m^2	1.08×10^{-7}	2.84×10^{-7}
σ_{effl}	S/m	31.9	8.32×10^{-4}
Li^+ flux$_{void-NMC}$	mol/m^2s	1.481×10^{-2}	7.44×10^{-3}
$i_{current\ collector}$	mA/mm^2	2.652	3.51
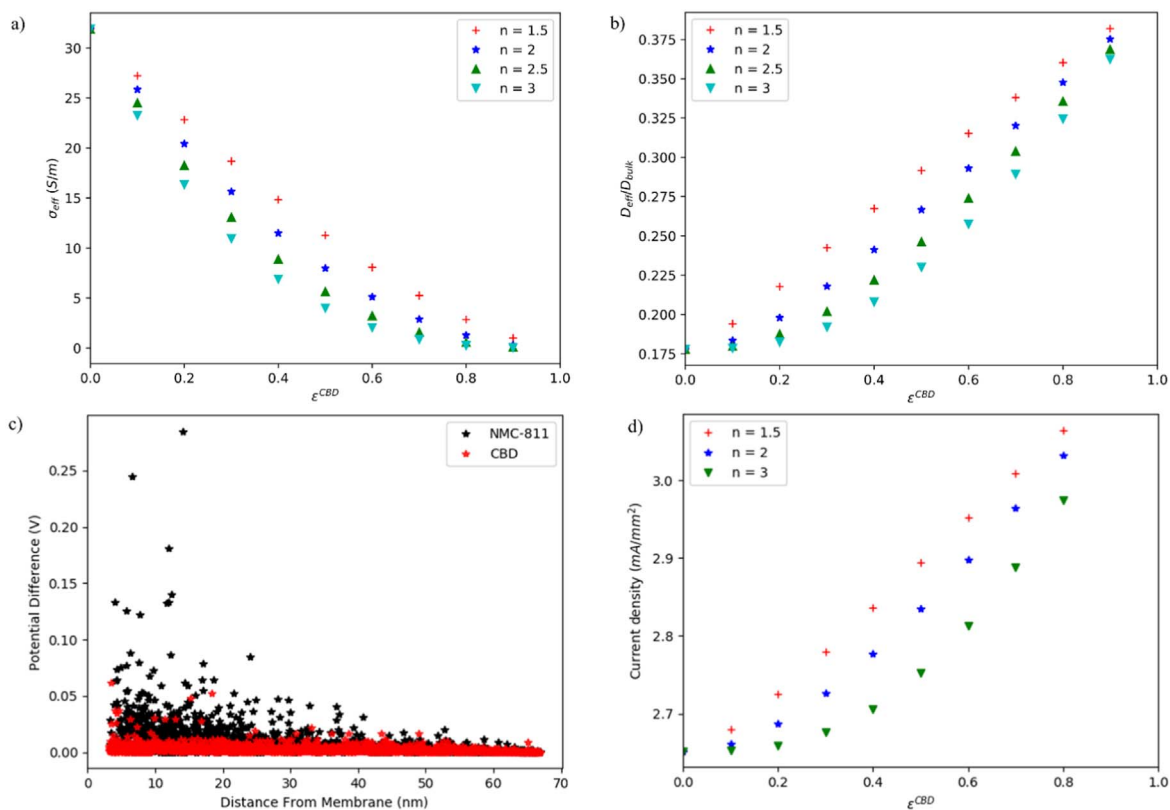
Figure 8. (a) Effective electronic conductivity of solid matrix (NMC + CBD) vs nanoporosity of CBD, (b) Effective diffusivity of Li-Ion in electrolyte phase vs nanoporosity of CBD, (c) Potential difference in solid matrix vs distance from membrane at $\varepsilon_{CB} = 0$ and $n = 3$, (d) Current density of solid matrix vs CBD nanoporosity.

image cropping, but the topology near the edges is unavoidable impacted and this could explain the observed voltages.

Figure 8d shows current density simulated at different ε_{CB} values. It can be seen that current density increases from 2.65 mA.mm^{-2} to 3.1 mA.mm^{-2} by changing the nanoporosity from 0 to 80% phase. This represents an 16.8% increase in maximum current density, but it must be conceded that simulation is not indicative of actual performance, since in reality the reaction rate would drop significantly in sites with a high ohmic overpotential due to the exponential dependence of electrochemical kinetics on voltage. The observed behavior is due to more available reaction area and more Li-ion pathways available from the electrolyte phase to active material due to the presence of nanopores in CBD. The loss of electrical conductivity is not factored into this result, and it is quite likely that a peak in current would be observed as some intermediate value of ε_{CBD}, though this is outside the scope of the present work.

Conclusions

In this work, a pore network extraction algorithm was developed to extract connectivity and geometrical information from a ternary X-ray tomography image of a three-phase lithium nickel manganese cobalt oxide ($LiNi_{0.8}Mn_{0.1}Co_{0.1}O_2$) porous cathode. The extracted three-phase network not only includes geometric information of each phase but also topological information such as the interlinking of all phases with themselves and each other. This enables the study of pore-scale transport through the structure while considering the transport process in each phase.

For validation, effective transport properties including the effective diffusivity of the pore phase and effective conductivity of the solid phase were calculated using DNS as a reference solution, and results compared favorably with the extracted network. Once the model was validated, more sophisticated simulations were performed by considering reaction-diffusion and reaction-conduction process in electrolyte and solid phase of three-phase network. These studies mimicked battery operation for the limiting case of maximum current, since only diffusion in the electrolyte phase and very fast kinetics at the electrolyte-active material interface were considered. This revealed that the maximum currents that can be supported by the electrode structure are substantially higher than experimentally observed currents.

The developed pore network model was used in two case studies to highlight the effect of incorporating nanopores in the carbon binder phase, as well as the importance of using three-phase network over two-phase network of Lithium-ion battery. The results showed a 24.4% decrease in current density when the carbon binder was treated as a separate phase compared to lumping the CBD and active material into a single phase, as is often done in previous pore-scale

simulations on binary images. Moreover, it was observed that ionic and electronic transport properties are affected by inclusion of nanopores in the carbon binder phase. The current density was observed to increase by 16.8% as the nano-porosity of CBD increases from 0 to 80%.

As compared to direct numerical simulation, the present work uses relatively large electrode domain to model multiple coupled phases together in a computationally efficient way. With the increased ability to stitch larger regions of electrode images together and decreasing data acquisition time, the approach explored here will become increasingly necessary in order to accurately describe realistic Li-ion battery electrodes and the inhomogeneities that can be present across their entire area. Also, the current study focuses only on steady-state processes, but due to low computational cost of pore network models, a transient approach to simulate porous media can be adopted.

Acknowledgments

ORCID

Zohaib Atiq Khan https://orcid.org/0000-0003-2115-7798
Pablo Angel Garcia Salaberri https://orcid.org/0000-0002-3918-5415
Thomas M. M. Heenan https://orcid.org/0000-0001-9912-4772
Paul R. Shearing https://orcid.org/0000-0002-1387-9531
Dan Brett https://orcid.org/0000-0002-8545-3126
Ali Elkamel https://orcid.org/0000-0002-6220-6288
Jeff T. Gostick https://orcid.org/0000-0001-7736-7124

References

1. M. Li, J. Lu, Z. Chen, and K. Amine, *Adv. Mater.*, **30**, 1800561 (2018).
2. J. Newman and W. Tiedemann, *AIChE J.*, **21**, 25 (1975).
3. Y. Chan and J. J. Wylie, *EPL (Europhysics Lett.)*, **123**, 14002 (2018).
4. K. Yoo, S. Banerjee, J. Kim, and P. Dutta, *Energies*, **10**, 1748 (2017).
5. T. Hutzenlaub, S. Thiele, N. Paust, R. Spotnitz, R. Zengerle, and C. Walchshofer, *Electrochim. Acta*, **115**, 131 (2014).
6. D. E. Stephenson, B. C. Walker, C. B. Skelton, E. P. Gorzkowski, D. J. Rowenhorst, and D. R. Wheeler, *J. Electrochem. Soc.*, **158**, A781 (2011).
7. A. G. Kashkooli, A. Amirfazli, S. Farhad, D. U. Lee, S. Felicelli, H. W. Park, K. Feng, V. De Andrade, and Z. Chen, *J. Appl. Electrochem.*, **47**, 281 (2017).
8. C. Tan, T. M. M. Heenan, R. F. Ziesche, S. R. Daemi, J. Hack, M. Maier, S. Marathe, C. Rau, D. J. L. Brett, and P. R. Shearing, *ACS Appl. Energy Mater.*, **1**, 5090 (2018).
9. Q. Meyer, N. Mansor, F. Iacoviello, P. L. Cullen, R. Jervis, D. Finegan, C. Tan, J. Bailey, P. R. Shearing, and D. J. L. Brett, *Electrochim. Acta*, **242**, 125 (2017).
10. M. Aghighi, M. A. Hoeh, W. Lehnert, G. Merle, and J. Gostick, *J. Electrochem. Soc.*, **163**, F384 (2016).
11. M. Aghighi and J. Gostick, *J. Appl. Electrochem.*, **47**, 1323 (2017).
12. M. El Hannach, M. Prat, and J. Pauchet, *Int. J. Hydrogen Energy*, **37**, 18996 (2012).
13. M. A. Sadeghi, M. Aganou, M. Kok, M. Aghighi, G. Merle, J. Barralet, and J. Gostick, *J. Electrochem. Soc.*, **166**, A2121 (2019).
14. A. Gayon Lombardo, B. A. Simon, O. Taiwo, S. J. Neethling, and N. P. Brandon, *J. Energy Storage*, **24**, 100736 (2019).
15. P. A. García-Salaberri, I. V. Zenyuk, A. D. Shum, G. Hwang, M. Vera, A. Z. Weber, and J. T. Gostick, *Int. J. Heat Mass Transf.*, **127**, 687 (2018).
16. P. A. García-Salaberri, I. V. Zenyuk, G. Hwang, M. Vera, A. Z. Weber, and J. T. Gostick, *Electrochim. Acta*, **295**, 861 (2019).
17. M. F. Lagadec, R. Zahn, S. Müller, and V. Wood, *Energy Environ. Sci.*, **11**, 3194 (2018).
18. A. Torayev, A. Rucci, P. C. M. M. Magusin, A. Demortière, V. De Andrade, C. P. Grey, C. Merlet, and A. A. Franco, *J. Phys. Chem. Lett.*, **9**, 791 (2018).
19. A. Torayev, P. C. M. M. Magusin, C. P. Grey, C. Merlet, and A. A. Franco, *ACS Appl. Energy Mater.*, **1**, 6433 (2018).
20. S. R. Daemi, C. Tan, T. Volkenandt, S. J. Cooper, A. Palacios-Padros, J. Cookson, D. J. L. Brett, and P. R. Shearing, *ACS Appl. Energy Mater.*, **1**, 3702 (2018).
21. Z. A. Khan, T. Tranter, M. Agnaou, A. Elkamel, and J. Gostick, *Comput. Chem. Eng.*, **123**, 64 (2019).
22. J. Gostick, Z. Khan, T. Tranter, M. Kok, M. Agnaou, M. Sadeghi, and R. Jervis, *J. Open Source Softw.*, **4**, 1296 (2019).
23. P. Soille, *Morphological Image Analysis* (Springer Berlin, Heidelberg) (2004), http://link.springer.com/10.1007/978-3-662-05088-0.
24. M. J. Blunt, *Multiphase Flow in Permeable Media* (Cambridge University Press, Cambridge) (2017), https://cambridge.org/core/books/multiphase-flow-in-permeable-media/455B5CA44AAF69F06A82DE091CD631C7..
25. J. T. Gostick, *Phys. Rev. E*, **96**, 023307 (2017).
26. J. Gostick et al., *Comput. Sci. Eng.*, **18**, 60 (2016).
27. J. Landesfeind and H. A. Gasteiger, *J. Electrochem. Soc.*, **166**, A3079 (2019).
28. A. Ehrl, J. Landesfeind, W. A. Wall, and H. A. Gasteiger, *J. Electrochem. Soc.*, **164**, A826 (2017).
29. Y.-H. Chen, C.-W. Wang, G. Liu, X.-Y. Song, V. S. Battaglia, and A. M. Sastry, *J. Electrochem. Soc.*, **154**, A978 (2007).
30. H.-J. Noh, S. Youn, C. S. Yoon, and Y.-K. Sun, *J. Power Sources*, **233**, 121 (2013).
31. F. L. E. Usseglio-Viretta et al., *J. Electrochem. Soc.*, **165**, A3403 (2018).
32. B. L. Trembacki, A. N. Mistry, D. R. Noble, M. E. Ferraro, P. P. Mukherjee, and S. A. Roberts, *J. Electrochem. Soc.*, **165**, E725 (2018).
33. L. Zielke, T. Hutzenlaub, D. R. Wheeler, C.-W. Chao, I. Manke, A. Hilger, N. Paust, R. Zengerle, and S. Thiele, *Adv. Energy Mater.*, **5**, 1401612 (2015).
34. B. Tjaden, S. J. Cooper, D. J. Brett, D. Kramer, and P. R. Shearing, *Curr. Opin. Chem. Eng.*, **12**, 44 (2016).
35. A. Mistry and P. P. Mukherjee, *Phys. Fluids*, **31**, 122005 (2019).